



Final Draft **of the original manuscript**

Jiang, P.; Blawert, C.; Bohlen, J.; Zheludkevich, M.:

Corrosion performance, corrosion fatigue behavior and mechanical integrity of an extruded Mg₄Zn_{0.2}Sn alloy.

In: Journal of Materials Science & Technology. Vol. 59 (2020) 107 – 116.

First published online by Elsevier: 20.06.2020

<https://dx.doi.org/10.1016/j.jmst.2020.04.042>

Corrosion performance, corrosion fatigue behavior and mechanical integrity of an extruded Mg4Zn0.2Sn alloy

Pingli Jiang^{a*}, Carsten Blawert^a, Jan Bohlen^a, Mikhail L. Zheludkevich^{a,b}

^a Magnesium Innovation Centre - MagIC, Institute of Materials Research, Helmholtz-Zentrum Geesthacht, Max-Planck Str.1, Geesthacht 21502, Germany

^b Faculty of Engineering, University of Kiel, Kaiserstrasse 2, 24143 Kiel, Germany

* Corresponding author:

Pingli Jiang, E-Mail: *pingli.jiang@hzg.de*

Magnesium alloys are promising as load bearing components. They are inevitably exposed to cyclic loading and corrosive environment in actual service, which can consequently result in corrosion fatigue failure and loss of mechanical integrity of the material. Therefore, in the present study, the corrosion behavior, corrosion fatigue performance and mechanical integrity of an extruded Mg4Zn0.2Sn (wt.%) alloy were thoroughly studied in two corrosive electrolytes. Strong localized corrosion occurred when the alloy was immersed in deionized water based sodium chloride (NaCl) solution. The poor corrosion resistance of the alloy resulted in the fast deterioration of the tensile properties after pre-exposure to salt spray and the poor fatigue resistance in deionized water based NaCl solution. In comparison, the active dissolution of the substrate was sufficiently suppressed in artificial tap water based NaCl solution due to the formation of highly protective corrosion product layers. This consequently conferred longer fatigue life on the alloy in the electrolyte. Our results emphasized the influence of corrosion on the fatigue behavior and tensile properties of magnesium alloys.

Keywords: Magnesium alloy; Tin. Artificial tap water; Corrosion fatigue; Mechanical integrity.

1. Introduction

1 Magnesium (Mg) alloys have attracted considerable attention for their promising applications
2 as load-bearing components in transportation and biomedical areas. They can inevitably
3 experience dynamic loading in actual service. For example, car wheels undergo cyclic
4 loading at elastic stress levels with several 10^8 cycles and cardiovascular stents suffer cyclic
5 stress induced by heart beats ^[1-3]. With the synergetic action of mechanical loading and
6 corrosive environment, corrosion assisted cracking can lead to the sudden premature failure
7 of the materials. The nature of loading results in different failure modes, including stress
8 corrosion cracking (SCC) induced by tensile loading and corrosion fatigue resulting from
9 cyclic loading ^[4, 5]. Up to now, SCC of Mg alloys has been extensively studied ^[3, 6-9], while
10 limited attention has been paid on the corrosion fatigue of Mg alloys ^[5]. Since catastrophic
11 failure can be caused by corrosion fatigue fracture, it is imperative to thoroughly investigate
12 the corrosion fatigue performance of Mg alloys before their practical applications as load-
13 bearing structural materials.

14 Generally, fatigue cracks initiate in air from solidification defects for as-cast Mg alloys and
15 from slip bands or twin boundaries for wrought Mg alloys ^[1]. In comparison, corrosion pits
16 are identified to be crack initiation sites when Mg alloys are tested in corrosive environment.
17 Moreover, different corrosive electrolytes can affect the nucleation and growth of the
18 corrosion pits and the consequent corrosion fatigue lives of Mg alloys ^[4]. Uematsu et al. ^[10]
19 studied the influence of controlled humidity on the fatigue crack propagation of AZ61 alloy.
20 The crack propagation rate was faster in humid atmosphere compared to that in dry air, even
21 at a low humidity of 20 % R.H., but was independent from the level of humidity. In
22 comparison with humid condition, much higher reduction of fatigue strength was revealed in
23 5 wt.% sodium chloride or calcium chloride solutions. This was a result of the enhanced
24 formation and growth of corrosion pits to the critical size for crack nucleation induced by
25 corrosive chloride ions, as demonstrated by the work of Bhuiyan et al ^[11]. Accordingly, with
26 enhanced resistance to pitting, improvement of corrosion fatigue behavior of Mg alloys can
27 be achieved ^[5]. Harandi et al. ^[12] compared the fatigue performance of AZ91D alloy in
28 Hank's solution with and without bovine serum albumin (BSA) and found that the fatigue
29 resistance of the alloy was higher in solution with BSA. This was attributed to the absorption
30 of BSA on the alloy surface, which suppressed the dissolution of the substrate.

31 Characterization of the mechanical properties of Mg alloys before exposure to the mimic or
32 actual service environment is the usual case for the majority of currently reported literature
33 ^[13-18]. However, the inevitable corrosion of Mg alloys in aggressive environment can cause
34 the deterioration of mechanical integrity during their service duration, especially when

1 localized corrosion occurs, which can significantly affect the support life of the material ^[19, 20].
2 Therefore, apart from the initial mechanical properties of an alloy, the mechanical integrity
3 should also be considered during the development of a novel alloy for commercial
4 application.

5 Recently, the magnesium-zinc-tin (Mg-Zn-Sn) system has drawn increasing attention for
6 potential applications as both structural components and biomaterials ^[21, 22]. Investigations
7 have been carried out on the influence of microstructure on the structure stability, mechanical
8 properties and corrosion performance of Mg-Zn-Sn alloys ^[22-27]. Studies show that the
9 mechanical properties of Mg-Zn-Sn alloys at elevated temperature are superior to those of the
10 conventional magnesium-aluminum series alloys ^[28]. Moreover, Mg-Zn-Sn alloys have been
11 considered as a promising high-strength precipitation-hardenable system ^[29, 30]. The reasons
12 for this are the relatively high solid solubility of Zn and Sn in Mg at high temperature ^[20, 31],
13 the precipitation of Mg-Zn transition phases during aging treatment ^[32-34] and the formation
14 of Mg₂Sn phase with high melting point ^[35]. Mg₄Zn (in *wt. %*) alloy has been reported to
15 possess a good combination of low corrosion rate, moderate mechanical properties and good
16 biocompatibility ^[20, 36]. With the addition of Sn, the mechanical properties of Mg₄Zn alloy
17 can be further enhanced, but the effect becomes minor when Sn content is increased from 1
18 *wt.%* to 2 *wt.%*. Moreover, 2 *wt.%* Sn can strongly deteriorate the corrosion performance of
19 Mg₄Zn alloy ^[22]. Consequently, micro addition (0.2 *wt.%*) of Sn is considered in this study.
20 In spite of the increasing interest in Mg-Zn-Sn system, no studies about the mechanical
21 integrity or fatigue/corrosion fatigue behavior of the alloy can be found.

22 Therefore, in this study, the corrosion performance, corrosion fatigue behavior and
23 mechanical integrity of an extruded Mg₄Zn0.2Sn (in *wt.%*) alloy were firstly
24 comprehensively studied, with an emphasis on the influence of corrosion on the fatigue
25 behavior and tensile properties. The fatigue behavior was compared in air and two different
26 corrosive solutions and the mechanical integrity was studied by exposing the samples to salt
27 spray for different time length. To have a good understanding upon these properties of the
28 extruded Mg₄Zn0.2Sn alloy, the microstructure, corrosion morphologies and fracture
29 surfaces after tensile or fatigue tests were analyzed.

30 **2. Experimental**

31 2.1 Material and solution preparation

32 The extruded Mg₄Zn0.2Sn (*wt.%*) alloy was prepared by indirect chill casting, then
33 homogenized at 320 °C for 24 h and finally extruded at 2.2 mm/s at 375 °C. The
34 homogenization treatment was applied to improve the extrudability of the alloy ^[37] and more

1 importantly to receive a well homogenized material with the alloying elements in solid
2 solution as much as possible. The temperature for the homogenization treatment and
3 extrusion process was chosen according to the Mg₄Zn-Sn phase diagram provided in our
4 another work ^[38], which is above the solvus temperature of precipitates. A rather low
5 extrusion speed of 2.2 mm/s has been applied to avoid additional deformation related heating
6 and grain coarsening as a result of enhanced dynamic recrystallization and grain growth. The
7 composition of the nominal Mg₄Zn_{0.2}Sn alloy is 0.17 % Sn, 3.77 % Zn, 0.028 % Mn,
8 0.0004 % Ni, 0.0069 % Si, 0.0014 % Cu, 0.0018 % Fe and balanced by Mg (all in *wt.%*),
9 which was determined by atomic absorption spectrometry (240FS AA, Agilent)
10 (determination of Sn) and spark optical emission spectroscopy (Spectrolab M9, Spectro
11 Ametek). Sodium chloride (NaCl) solutions (0.5 *wt.%*) prepared with deionized water (DIW)
12 and artificial tap water (ATW) ^[39] were used for the investigation of the corrosion behavior
13 and corrosion fatigue performance of the alloy. The former provided a simply simulated
14 condition while the latter presented a closer condition to the actual service environment of the
15 alloy. In the following texts, these two solutions are referred to as NaCl-DIW and NaCl-ATW,
16 respectively.

17 2.2 Microstructure characterization

18 Optical microscopy (OM) (Leica DM2500 M, Leica Microsystems) and scanning electron
19 microscopy (SEM) (Vega 3 SB, TESCAN Brno) were utilized to analyze the microstructure.
20 Samples were successively ground to 2500 grit with silicon carbide papers accompanied by
21 flowing water and subsequently mechanically polished in a mixture of non-aqueous silica
22 suspension and 1 μm diamond slurries. The second phases were characterized by using
23 backscattered electron mode (BSE) of SEM and an energy dispersive X-ray spectroscopy
24 (EDS) at a working voltage of 20 kV. Before observation with OM, the polished mirror
25 surface was etched by an etchant that was based on picric acid to reveal the grain boundaries.

26 2.3 Electrochemical measurements

27 Electrochemical impedance spectroscopy (EIS) and potentiodynamic polarization tests were
28 performed in NaCl-DIW and NaCl-ATW solutions to investigate the corrosion behavior of
29 Mg₄Zn_{0.2}Sn alloy. A Gill/AC potentiostat (Gill AC, ACM Instruments) was used for the
30 measurements. The three-electrode cell for the electrochemical tests was made up of an alloy
31 disc with 0.5 cm² exposed surface area, an Ag/AgCl electrode saturated with potassium
32 chloride solution and a platinum mesh, which served as the working, reference and counter
33 electrode respectively. The frequency for EIS tests ranged from 30000 Hz to 0.1 Hz at an AC
34 voltage disturbance of 10 mV rms. EIS tests lasted for 48 h with the acquisition of data at

1 certain time points. After immersion for 48 h, anodic and cathodic polarization curves were
2 acquired separately at a scanning rate of 0.5 mV s^{-1} . The anodic curves were measured from -
3 5 mV to 700 mV relative to the open circuit potential (OCP) and the cathodic ones were
4 obtained from 5 mV to - 400 mV versus OCP. All tests were carried out under magnetic
5 stirring and at least four tests were repeated. The face perpendicular to the extrusion direction
6 was used for all electrochemical measurements and the following immersion tests.

7 2.4 Corrosion products analysis

8 To facilitate the understanding of the corrosion behavior of Mg₄Zn_{0.2}Sn alloy, immersion
9 tests were performed in NaCl-DIW and NaCl-ATW solutions for 48 h. The surface and cross
10 section morphologies after corrosion were examined by SEM in BSE mode. Additionally, the
11 detailed compositions of the corrosion products formed in different solutions were
12 determined by X-ray diffraction (XRD) (D8 Advance, Bruker) with Cu K α radiation. The
13 diffraction patterns were collected from 15° to 85° with 0.01° per step and 2 s for each step at
14 40 kV and 40 mA.

15 2.5 Texture analysis

16 Six pole figures of the Mg₄Zn_{0.2}Sn alloy were recorded using XRD to determine the texture.
17 The measurements were carried out at 40 kV on the sample surface perpendicular to the
18 extrusion direction and up to a sample tilt of 70° . An MTEX toolbox ^[40] was used to analyze
19 the obtained data and to reveal the inverse pole figure parallel to the extrusion direction in
20 order to reveal the orientation distribution of the sample.

21 2.6 Mechanical tests

22 The tensile and compressive properties of Mg₄Zn_{0.2}Sn alloy were evaluated by a materials
23 tensile testing machine (Zwick/Roell Z050, Zwick GmbH & Co KG) at room temperature.
24 The strain rate was 10^{-3} s^{-1} . To investigate the mechanical integrity (only tensile properties) of
25 Mg₄Zn_{0.2}Sn alloy, specimens were exposed to salt spray using ASTM B117 standard for
26 different time intervals. Bee wax was used to protect the screw threads from corrosion for the
27 subsequent tensile tests after pre-corrosion. Macroscopic surface appearance of specimens
28 after salt spray was recorded by OM. Afterwards, tensile tests were carried out with the
29 corroded specimens. For statistic purpose, at least three samples were measured. After the
30 tensile tests, the fractured surfaces were checked by SEM.

31 2.7 Fatigue and corrosion fatigue tests

32 An electrodynamic test system (MTS Acumen, MTS Systems Corporation) was utilized to
33 study the fatigue behavior of Mg₄Zn_{0.2}Sn alloy. The frequency for the axial sinusoidal
34 loading was 30 Hz. The measurement was not stopped unless the sample failed. If the

1 specimen survived at one stress amplitude for up to 10^7 cycles then the measurement was
2 stopped automatically. Consequently, this stress level was defined as the fatigue limit of the
3 alloy. Fractural morphologies were studied by SEM to examine the growth of fatigue cracks.

4 **3. Results**

5 3.1 Microstructure and texture analysis

6 The grain structure of the extruded Mg₄Zn_{0.2}Sn alloy reveals typical equiaxial
7 characteristics, as shown in Fig. 1a, with an average size of $34 \pm 1 \mu\text{m}$. It implies that
8 dynamic recrystallization almost fully completed during the extrusion process. The SEM
9 images (Fig. 1b and 1c) show that element segregation occurs in the alloy and some fine
10 precipitates exist at the grain boundaries while a few larger particles precipitate inside the
11 grains. Those larger particles are Fe-Mn/SiO₂ impurities according to the EDS analysis [38].
12 The recalculated inverse pole figure (Fig. 1d) exhibits a distinct alignment of basal planes
13 along the extrusion direction, which has been commonly revealed for extruded Mg alloys [41,
14 42]. In addition, the highest intensity at the <11-20> pole (upper right in the inverse pole figure)
15 is in good agreement with the recrystallized nature of the microstructure [43].

16 3.2 Corrosion performance in different solutions

17 To monitor the corrosion behavior of Mg₄Zn_{0.2}Sn alloy and the state of the surface during
18 immersion in NaCl-DIW and NaCl-ATW solutions, EIS tests were continuously conducted
19 for 48 h. Besides, polarization curves separately taken from the OCP to cathodic and anodic
20 directions were collected to investigate the formation of surface layers in different solutions.
21 Furthermore, the corrosion products were further examined to reveal the corrosion
22 mechanism of the alloy in different corrosive media.

23 3.2.1 EIS measurements

24 Fig. 2 compares the impedance spectra (in Bode plots) of Mg₄Zn_{0.2}Sn alloy in NaCl-DIW
25 and NaCl-ATW solutions. When exposed to NaCl-DIW solution (Fig. 2a and b), the
26 impedance value decreases after immersion for 5 min (i.e. as soon as the test started) and then
27 fluctuates at around $500 \Omega \text{ cm}^2$ after exposure for more than 8 h. Interestingly, in NaCl-ATW
28 solution (Fig. 2c and d), the impedance value gradually increases with prolonged exposure
29 and is significantly higher than that measured in NaCl-DIW solution after 24 h. Two time
30 constants can be observed in the initial hours (less than 12 h), while the one located in the
31 low frequency region becomes less and less visible with immersion time. The totally different
32 impedance response of the alloy in NaCl-DIW and NaCl-ATW solutions suggests that
33 different surface layers are formed on the alloy surface.

1 3.2.2 Potentiodynamic polarization

2 Distinct difference can be observed between the potentiodynamic polarization curves (Fig. 3)
3 of the alloy measured in NaCl-DIW and NaCl-ATW solutions. Firstly, the corrosion current
4 density (i_{corr}) tested in NaCl-DIW solution is significantly higher compared to that measured
5 in NaCl-ATW solution, indicating that the corrosion resistance of the alloy in NaCl-DIW
6 solution is poorer than in NaCl-ATW solution. Secondly, for the anodic curves, the current
7 density steeply increases with applied potential in NaCl-DIW solution while it is apparently
8 retarded in NaCl-ATW solution, exhibiting a plateau region. This implies that a protective
9 surface layer is formed in NaCl-ATW solution and suppresses the anodic dissolution of
10 Mg₄Zn_{0.2}Sn alloy. While the surface layer formed in NaCl-DIW solution is almost non-
11 protective. This agrees well with the EIS results.

12 3.2.3 Corrosion morphologies and products analysis

13 Fig. 4a and 4c show that Mg₄Zn_{0.2}Sn alloy is subjected to localized corrosion in NaCl-DIW
14 solution after immersion for 48 h, exhibiting obvious localized attack of the surface. While in
15 NaCl-ATW solution, uniform surface morphology (Fig. 4b) is revealed. The substrate is
16 covered by tightly arranged flower-like corrosion products. Notably, the flower-like products
17 form an additional compact layer on the surface of the alloy (Fig. 4d). In contrast, the layer of
18 corrosion products formed in NaCl-DIW solution is not dense (Fig. 4c). This explains the
19 dissimilar impedance and polarization responses of the alloy in NaCl-DIW and NaCl-ATW
20 solutions.

21 According to the diffraction patterns shown in Fig. 5, magnesium hydroxide (Mg(OH)₂) is
22 the main corrosion products after Mg₄Zn_{0.2}Sn alloy exposed to NaCl-DIW solution for 48 h,
23 while calcium carbonate (CaCO₃) in the crystallographic form of aragonite predominates in
24 the case of NaCl-ATW solution. Considering the surface and cross section morphologies, the
25 flower-like corrosion products should be CaCO₃.

26 3.3 Mechanical properties and integrity

27 Fig. 6 shows the tensile and compressive stress-strain curves of Mg₄Zn_{0.2}Sn alloy measured
28 at ambient temperature, with the detailed properties displayed in Table 1. The tensile yield
29 strength (TYS), ultimate tensile strength (UTS) and elongation to fracture of the alloy are 157
30 MPa, 254 MPa and 16 %, respectively. However, a relatively high tension-compression yield
31 asymmetry of 2.0 is revealed.

32 The tensile curves after pre-corrosion and the variation of tensile properties with pre-
33 corrosion duration are displayed in Fig. 7 and summarized in Table 2, with comparison to the

1 unexposed alloy as well. The data for samples after pre-corrosion in salt fog for 42 days is
2 missing because the corrosion of the samples was so severe that the bee wax has lost its
3 protective function and thus the corroded screw thread did not allow a tensile test anymore.
4 As revealed, the tensile properties of Mg₄Zn_{0.2}Sn alloy gradually declines with prolonged
5 pre-corrosion duration. After 28 days, the TYS, UTS and elongation to fracture decrease to
6 be 136 MPa, 189 MPa and 4 %, showing a reduction of 13 %, 26 % and 75 % compared with
7 those of the uncorroded alloy, respectively. Apparently, the elongation to fracture suffers the
8 greatest reduction.

9 Fig. 8 reveals the surface appearance of Mg₄Zn_{0.2}Sn alloy after pre-corrosion for 3 days, 14
10 days, 28 days and 42 days in salt spray. Notably, localized attack already occurs after only 3
11 days, which becomes increasingly intense with further exposure in salt spray, indicated by the
12 formation of more and more white corrosion product aggregates.

13 Furthermore, the fracture surfaces after tensile tests were also examined to get an insight into
14 the deterioration of mechanical properties under the influence of salt fog exposure, as shown
15 in Fig. 9. The first, second and third columns display the overall fracture appearance in BSE
16 images, enlarged fracture details in SE pictures and in BSE images, respectively. In
17 accordance with the macroscopic morphologies in Fig. 8, the overall images of the fractures
18 (Fig. 9a, 9d, 9g, 9j) show that thicker corrosion product layers are forming on the sample
19 surfaces as the pre-corrosion duration prolongs. Meanwhile, localized corrosion cavities
20 increase, expand and/or grow deeper inside the material. For the bare alloy (Fig. 9b), the
21 fracture surface discloses a mixed characteristic, dominated by tear ridges with some dimples
22 and cleavages. Similar fracture feature is also observed for the fracture surfaces of pre-
23 corroded Mg₄Zn_{0.2}Sn alloy (Fig. 9e, 9h and 9k) despite the corrosion attack by salt fog.
24 However, more tear ridges and less dimples are noticed, especially after pre-corrosion for 28
25 days, indicating that the fracture becomes less ductile but more brittle. In accordance with the
26 microstructure revealed in Fig. 1b and 1c, a few bright particles are observed in the fracture
27 surfaces when imaged by BSE mode (Fig. 9c, 9f, 9i, 9l).

28 3.4 Fatigue and corrosion fatigue behavior

29 The stress-life cycle (S-N) curves of Mg₄Zn_{0.2}Sn alloy tested in air, NaCl-DIW and NaCl-
30 ATW solutions are displayed in Fig. 10. In air, the fatigue lives extend moderately with the
31 reduction of applied load and eventually reach the fatigue limit at a stress amplitude of 150
32 MPa. A horizontal region exists from 10⁵ to 10⁷ cycles. When the samples are exposed to
33 corrosive electrolytes (NaCl-DIW and NaCl-ATW solutions) under a stress level at or lower
34 than the fatigue limit in air, the fatigue lives significantly decrease. Even under a much lower

1 stress amplitude (as low as 120 MPa), no fatigue limits are detected in the corrosive solutions.
2 Additionally, it is worth noting that the S-N curve of Mg₄Zn_{0.2}Sn alloy in NaCl-DIW
3 solution is highly scattered, while it is not the case in NaCl-ATW solution. This may be
4 related to the varied corrosion performance of the alloy in these two solutions as revealed
5 above.

6 Fig. 11 depicts the fracture surfaces of Mg₄Zn_{0.2}Sn alloy after fatigue failure in air and in
7 NaCl-DIW and NaCl-ATW solutions at a stress amplitude below the fatigue limit in air. The
8 overall fracture morphologies shown in the first column (Fig. 11a, 11e and 11i) reveal three
9 apparent regions: crack initiation region, crack propagation region and the overload tearing
10 region. The yellow arrows in Fig. 11a, 11e and 11i indicate the direction of the crack
11 propagation. The remained three columns display the three corresponding regions with
12 enlarged details. Firstly, for the crack regions, dark aggregates (denoted by yellow arrows in
13 Fig. 11b) seem to trigger the fatigue crack in air. While obvious corrosion pits (as revealed by
14 the inserted pictures in Fig. 11f and 11j after removal of corrosion products) turn out to be the
15 initiators of the cracks in NaCl solutions when the applied load was below the fatigue limit in
16 air. This is especially apparent in NaCl-DIW solution when the specimen failed after a
17 relatively long life cycle (about 24 h). EDS analysis in Fig. 12 demonstrates that those
18 aggregates in Fig. 11b are rich in oxygen (O) and carbon (C) with a small amount of Ca,
19 potassium (K), Cl, sulphur (S), and silicon (Si), which should be inclusions resulting from the
20 raw materials or the casting procedure. Actually, when tested at the stress amplitude of the
21 fatigue limit in air, cracks also initiate from those inclusions irrespective of the electrolytes.
22 This indicates the accelerated fatigue cracking of the alloy or the magnified crack initiator
23 roles of microstructural defects in corrosive solutions, which has been revealed in our
24 previous study ^[39]. The crack propagation regions (Fig. 11c, 11g and 11k) show similar
25 characteristics under different testing conditions, featured by brittle cleavages composed of
26 fine steps. For the overload tearing regions, the fracture surfaces formed in air and in NaCl-
27 DIW solution are similar to the fracture surfaces after tensile tests, showing many tear ridges
28 with a few dimples. In the case of NaCl-ATW solution, the corrosion products result in the
29 less-defined surface morphology due to a delayed disassembly of the sample after fatigue
30 failure.

31 To understand the substantially scattered behavior of the S-N curve of Mg₄Zn_{0.2}Sn alloy in
32 NaCl-DIW solution, the fracture surfaces formed after different fatigue life cycles at 120
33 MPa were examined by SEM, as shown in Fig. 13. It is revealed that inclusions (indicated by
34 yellow arrows) seem to trigger the cracks, resulting in the fast fatigue failure of the sample

1 due to the relatively high amount of those inclusions. While in the other cases, corrosion pits
2 (indicated by red arrows) are the sources of fatigue cracks. More or bigger pits are formed
3 when the sample failed after higher life cycles.

4 **4. Discussion**

5 Generally, in the process of hot extrusion, dynamic recrystallization, dynamic precipitation
6 and plastic deformation occur concurrently. As a result, fine recrystallized grains, tiny
7 precipitates and strong alignment of crystal orientation along basal plane (strong basal texture)
8 would be developed [37]. Accordingly, an almost fully recrystallized microstructure with fine
9 equiaxial grains and tiny second phases as well as the preferential orientation of basal plane
10 parallel to the extrusion direction were revealed for the extruded Mg₄Zn_{0.2}Sn alloy.

11 Mg alloys are prone to dissolution when exposed to aggressive electrolyte, for example, NaCl
12 solution, due to the significantly electronegative potential of Mg and the inadequate corrosion
13 protection ability of the surface film [44]. Moreover, the inhomogeneous chemical distribution
14 of alloying elements (compositional inhomogeneity) in the microstructure can generate
15 micro-galvanic effects, leading to localized corrosion or pitting corrosion [45]. The
16 compositional inhomogeneity of the studied Mg₄Zn_{0.2}Sn alloy includes the formation of tiny
17 second phases, the impurity particles and the segregation of alloying elements.

18 In NaCl-DIW solution, all of those compositional inhomogeneity can contribute to localized
19 corrosion behavior of the alloy. During immersion, the general dissolution process of Mg can
20 be described as:



22 As a result, Mg(OH)₂, besides a thin magnesium oxide (MgO) film formed in air (not
23 detected by XRD in this study), is the predominant corrosion product formed in NaCl-DIW
24 solution. However, the remaining solubility of the MgO/Mg(OH)₂ surface film and the attack
25 of aggressive chloride ions (Cl⁻) in the solution can result in some defects of the corrosion
26 product film, thereby encouraging the occurrence of localized corrosion. The concomitant
27 alkalization of the solution near the sample surface in return leads to the formation of
28 Mg(OH)₂. Consequently, a fluctuation of the impedance value was observed in NaCl-DIW
29 solution. In this case, the electrochemical nature of the alloy dominates the corrosion
30 behavior.

31 In NaCl-ATW solution, in the presence of abundant calcium ions (Ca²⁺) and bicarbonate ions
32 (HCO₃⁻), the precipitation of CaCO₃, shown as following, is facilitated near the sample
33 surface due to the alkalization of the solution resulting from Mg dissolution:



3 Therefore, insoluble CaCO_3 products precipitate on the top of the inner $\text{MgO}/\text{Mg}(\text{OH})_2$ layer.
4 With extended exposure of the alloy to NaCl -ATW solution, the CaCO_3 layer gradually
5 grows to be more intact and thicker, which imparts good corrosion protection to the
6 underlying substrate, giving rise to a continuously increasing and higher impedance values.
7 As revealed by the EIS and immersion results, $\text{Mg}_4\text{Zn}_0.2\text{Sn}$ alloy suffered from serious
8 localized corrosion in NaCl solution. The initial fast dissolution of the substrate produces
9 sufficient Mg^{2+} at the solution/alloy interface, which favors the CaCO_3 crystallisation as
10 aragonite instead of the thermodynamically stable calcite polymorph [46-51]. Formation of
11 aragonite flowers on Mg alloys surface has been reported when pure Mg and ZM21 alloy are
12 immersed in Ringer's solution (containing CaCl_2 and NaHCO_3) [52]. In our previous study [53],
13 we have revealed that mixed polymorphs of CaCO_3 were formed on Mg alloy surface when
14 immersed in tap water based NaCl solution. Thus, the single-phase product of aragonite
15 formed in this study should be an outcome of two aspects: one is the poorer corrosion
16 property of the currently studied $\text{Mg}_4\text{Zn}_0.2\text{Sn}$ alloy; another is the much higher
17 concentration of HCO_3^- in the artificial tap water.

18 The tensile properties of the present $\text{Mg}_4\text{Zn}_0.2\text{Sn}$ alloy (TYS: 157 MPa, UTS: 254 MPa,
19 elongation to fracture: 16 %) are comparable to those of commercial AZ series alloys [54].
20 Moreover, compared with the extruded $\text{Mg}_4\text{Zn}_x\text{Sn}$ ($x= 1.0; 1.5; 2.0$, in wt.%) alloys studied
21 by Jiang et al. [22], our extruded $\text{Mg}_4\text{Zn}_0.2\text{Sn}$ alloy possesses higher strength despite the
22 much lower concentration of Sn, higher extrusion temperature (extrusion speed was not
23 provided in the reference) and the missing possible strengthening effect of precipitated
24 Mg_2Sn phases in this study. With the strong basal texture, a high tensile strength would be
25 reached when extruded Mg alloy is tensile tested parallel to the extrusion direction because of
26 the low Schmid factor for extension twinning and basal slip. In contrast, deformation
27 twinning is readily operative due to the compression along the basal plane when the alloy is
28 compressively tested along the extrusion direction, giving rise to low compressive strength
29 [37]. As such, a significant mechanical anisotropy (TYS/CYS) is revealed for the extruded
30 $\text{Mg}_4\text{Zn}_0.2\text{Sn}$ alloy.

31 With pre-corrosion for the sample before the tensile test, the actual sectional area for tensile
32 test would decrease because of the dissolution of the material, as disclosed by the overall
33 fracture surfaces in the first column of Fig. 9. This case became more severe with prolonged
34 exposure of the alloy to salt spray, leading to the gradual reduction of the tensile properties.

1 In addition, the occurrence of localized corrosion can induce stress concentration at those
2 corroded places, which favors the formation of cracks and embrittlement during tensile test.
3 Moreover, the byproduct hydrogen resulting from the dissolution of the substrate can
4 additionally induce embrittlement. As a result, after pre-corrosion for 28 days, the tensile
5 properties of Mg₄Zn_{0.2}Sn alloy were significantly deteriorated.
6 Under cyclic loading in air, cracks can be initiated from microstructural defects, such as
7 inclusions and micro-pores from the manufacturing process, intermetallics and slip bands etc.
8 [4, 55, 56], leading to the fatigue failure of the material. Considering the tiny size of the second
9 phases in Mg₄Zn_{0.2}Sn alloy, inclusions were identified to be the crack triggers in air. In
10 corrosive environment, both corrosion pits and those pre-existing microstructural defects can
11 lead to fatigue cracking [56]. Moreover, the fatigue failure of the material can be accelerated
12 due to the combined effect of fatigue and environment. Besides, the crack initiation role of
13 the microstructural defects can be magnified. At high stress amplitude, microstructural
14 defects can dominate as crack initiators because there is not enough time for the corrosion pits
15 to develop into the critical size for fatigue cracking. As a result, Mg₄Zn_{0.2}Sn alloy failed
16 quickly in both corrosive electrolytes and inclusions were identified as crack initiators when
17 tested at the stress amplitude of the fatigue limit in air (150 MPa). Lower stress amplitude
18 allows longer testing duration (longer fatigue life of the material). The persistent cyclic
19 loading would damage the surface film, thereby facilitating the penetration of aggressive
20 electrolytes towards the inner substrate and favoring the formation of localized corrosion pits.
21 Under such circumstance, the crack propagation rate accelerated by the corrosion pits is much
22 faster than that facilitated by the inclusions once they grow into the critical size.
23 Consequently, corrosion pits turned out to be the crack triggers when Mg₄Zn_{0.2}Sn alloy was
24 tested below 150 MPa in both solutions. Given the poor chemical inhomogeneity, especially
25 the segregation of elements, and the consequent poor corrosion property, the fatigue
26 resistance of Mg₄Zn_{0.2}Sn alloy is really sensitive in NaCl-DIW solution due to the active
27 dissolution of the material, exhibiting a quite scattered behavior even when the load was low.
28 Besides, the non-protective surface layer formed in NaCl-DIW also contributes to the poor
29 fatigue resistance of Mg₄Zn_{0.2}Sn alloy in the solution. In comparison, in NaCl-ATW
30 solution, the dissolution of the alloy was sufficiently retarded owing to the formation of an
31 additional protective CaCO₃ layer. Accordingly, the fatigue life of the alloy is much less
32 scattered and longer compared to that in NaCl-DIW solution.

33 **5. Conclusion**

1 In this study, the corrosion performance, corrosion fatigue behavior and mechanical integrity
2 of an extruded Mg₄Zn_{0.2}Sn alloy were comprehensively investigated. Our studied alloy
3 exhibited higher tensile strength than those reported Mg₄Zn_xSn alloys with higher content of
4 Sn. The significant compositional inhomogeneity resulted in the poor corrosion behavior of
5 the alloy, i.e. severe localized corrosion in deionized water based NaCl solution. Such poor
6 corrosion property consequently gave rise to the fast deterioration of tensile properties after
7 pre-corrosion in salt spray and poor fatigue resistance in deionized water based NaCl solution.
8 However, in artificial tap water based NaCl solution, the dissolution of the alloy was
9 significantly suppressed due to the formation of a highly protective corrosion product layer of
10 CaCO₃, which also improved the corrosion fatigue behavior of the alloy in this solution
11 compared to the deionized water based solution.

12 **Declaration of interests**

13 The authors declare that there is no conflict of interests.

14 **Data availability**

15 The raw/processed data required to reproduce these findings cannot be shared at this time as
16 the data also forms part of an ongoing study.

17 **Acknowledgement**

18 The author Pingli Jiang (CSC No. 201606310043) would like to thank the financial support
19 from China Scholarship Council (CSC). The technical support from Mr. Ulrich Burmester,
20 Mr. Volker Heitmann and Dr. Gerrit Kurz and the general discussion from our colleagues in
21 the Division of Corrosion and Surface Technology department is gratefully acknowledged.

23 **Reference**

- 24 [1] B.J. Wang, D.K. Xu, S.D. Wang, E.H. Han, *Front. Mech. Eng.*, 14 (2019) 113-127.
- 25 [2] R.K.S. Raman, L. Choudhary, *Emerging Materials Research*, 2 (2013) 219-228.
- 26 [3] L. Choudhary, R.K.S. Raman, *Acta Biomater.*, 8 (2012) 916-923.
- 27 [4] R.K.S. Raman, S. Jafari, S.E. Harandi, *Eng. Fract. Mech.*, 137 (2015) 97-108.
- 28 [5] S. Jafari, R.K.S. Raman, C.H.J. Davies, *Eng. Fract. Mech.*, 137 (2015) 2-11.
- 29 [6] M.B. Kannan, R.K.S. Raman, *Scripta Mater.*, 59 (2008) 175-178.

- 1 [7] L. Choudhary, J. Szmmerling, R. Goldwasser, R.K.S. Raman, *Procedia Engineer.*, 10 (2011)
2 518-523.
- 3 [8] L. Choudhary, R.K.S. Raman, *Eng. Fract. Mech.*, 103 (2013) 94-102.
- 4 [9] L. Choudhary, R.K.S. Raman, *Mater. Sci. Forum*, 690 (2011) 487-490.
- 5 [10] Y. Uematsu, T. Kakiuchi, M. Nakajima, Y. Nakamura, S. Miyazaki, H. Makino, *Int. J.*
6 *Fatigue*, 59 (2014) 234-243.
- 7 [11] M.S. Bhuiyan, Y. Mutoh, T. Murai, S. Iwakami, *Int. J. Fatigue*, 30 (2008) 1756-1765.
- 8 [12] S.E. Harandi, R.K.S. Raman, *Eng. Fract. Mech.*, 186 (2017) 134-142.
- 9 [13] B. Song, N. Guo, T.T. Liu, Q.S. Yang, *Mater. Des. (1980-2015)*, 62 (2014) 352-360.
- 10 [14] Y.F. Wang, F. Zhang, Y.T. Wang, Y.B. Duan, K.J. Wang, W.J. Zhang, J. Hu, *Mater. Sci.*
11 *Eng. A*, 745 (2019) 149-158.
- 12 [15] C.H. Hou, F.G. Qi, Z.S. Ye, N. Zhao, D.F. Zhang, X.P. Ouyang, *Mater. Sci. Eng. A*,
13 (2020) 138933.
- 14 [16] B. Li, B.G. Teng, G.X. Chen, *Mater. Sci. Eng. A*, 744 (2019) 396-405.
- 15 [17] L. Xiao, G.Y. Yang, J.M. Chen, S.F. Luo, J.H. Li, W.Q. Jie, *Mater. Sci. Eng. A*, 744
16 (2019) 277-289.
- 17 [18] Z. Zareian, M. Emamy, M. Malekan, H. Mirzadeh, W.J. Kim, A. Bahmani, *Mater. Sci.*
18 *Eng. A*, (2020) 138929.
- 19 [19] R.Q. Hou, J. Victoria-Hernandez, P.L. Jiang, R. Willumeit-Römer, B. Luthringer-
20 Feyerabend, S.B. Yi, D. Letzig, F. Feyerabend, *Acta Biomater.*, 97 (2019) 608-622.
- 21 [20] S.X. Zhang, X.N. Zhang, C.L. Zhao, J.N. Li, Y. Song, C.Y. Xie, H.R. Tao, Y. Zhang,
22 Y.H. He, Y. Jiang, Y.J. Bian, *Acta Biomater.*, 6 (2010) 626-640.
- 23 [21] G.H. Zhang, J.H. Chen, H.G. Yan, B. Su, X. He, M. Ran, *J. Alloy. Compd.*, 592 (2014)
24 250-257.
- 25 [22] W.Y. Jiang, J.F. Wang, W.K. Zhao, Q.S. Liu, D.M. Jiang, S.F. Guo, *J. Magnes. Alloy.*, 7
26 (2019) 15-26.

- 1 [23] S.H. Wei, T.P. Zhu, M. Hodgson, W. Gao, *Mater. Sci. Eng. A*, 585 (2013) 139-148.
- 2 [24] X.B. Liu, D.Y. Shan, Y.W. Song, R.S. Chen, E.H. Han, *Electrochim. Acta*, 56 (2011)
3 2582-2590.
- 4 [25] S. Cohen, G.R. Goren-Muginstein, S. Avraham, G. Dehm, M. Bamberger, in:
5 *Magnesium: Proceedings of the 6th International Conference on Magnesium Alloys and*
6 *Their Applications*, Wolfsburg, Germany, September 25-30, 2004.
- 7 [26] S. Cohen, G.R. Goren-Muginstein, S. Avraham, G. Dehm, M. Bamberger, in:
8 *Magnesium Technology. 5th Annual Symposium held at the TMS Annual Meeting*, Charlotte,
9 North Carolina, U.S.A., March 301-305, 2004.
- 10 [27] C.M. Wang, Y.G. Chen, S.F. Xiao, W.C. Ding, X. Liu, *Rare Metal Mat. Eng.*, 42 (2013)
11 2019-2022.
- 12 [28] K.R. Ravi, *T. Indian I Metals*, 68 (2015) 1081-1086.
- 13 [29] T.T. Sasaki, J.D. Ju, K. Hono, K.S. Shin, *Scripta Mater.*, 61 (2009) 80-83.
- 14 [30] S. Harosh, L. Miller, G. Levi, M. Bamberger, *J. Mater. Sci.*, 42 (2007) 9983-9989.
- 15 [31] H.M. Liu, Y.G. Chen, Y.B. Tang, S.H. Wei, G. Niu, *J. Alloy. Compd.*, 440 (2007) 122-
16 126.
- 17 [32] C.L. Mendis, K. Oh-Ishi, K. Hono, *Scripta Mater.*, 57 (2007) 485-488.
- 18 [33] C.J. Bettles, M.A. Gibson, K. Venkatesan, *Scripta Mater.*, 51 (2004) 193-197.
- 19 [34] J.B. Clark, *Acta Metall. Mater.*, 13 (1965) 1281-1289.
- 20 [35] T.T. Sasaki, K. Oh-Ishi, T. Ohkubo, K. Hono, *Scripta Mater.*, 55 (2006) 251-254.
- 21 [36] B.P. Zhang, Y. Wang, L. Geng, in: R. Pignatello (Ed.), *Biomaterials-Physics and*
22 *Chemistry*, InTech, Croatia, 2011, pp. 183-204.
- 23 [37] Z.R. Zeng, N. Stanford, C.H.J. Davies, J.F. Nie, N. Birbilis, *Int. Mater. Rev.*, 64 (2019)
24 27-62.
- 25 [38] P.L. Jiang, C. Blawert, N. Scharnagl, J. Bohlen, M.L. Zheludkevich, *Mechanistic*
26 *understanding of the corrosion behavior of Mg₄Zn_{0.2}Sn alloys: from the perspective view of*
27 *microstructure*, *Corros. Sci.*, (2020), Submitted.

- 1 [39] P.L. Jiang, C. Blawert, R.Q. Hou, J. Bohlen, N. Konchakova, M.L. Zheludkevich, Mater.
2 Des., 185 (2020) 108285.
- 3 [40] F. Bachmann, R. Hielscher, H. Schaeben, Solid State Phenom., 160 (2010) 63-68.
- 4 [41] N. Stanford, D. Atwell, A. Beer, C. Davies, M.R. Barnett, Scripta Mater., 59 (2008) 772-
5 775.
- 6 [42] B.P. Zhang, Y. Wang, L. Geng, C.X. Lu, Mater. Sci. Eng. A, 539 (2012) 56-60.
- 7 [43] S.B. Yi, H.-G. Brokmeier, D. Letzig, J. Alloy. Compd., 506 (2010) 364-371.
- 8 [44] K. Gusieva, C.H.J. Davies, J.R. Scully, N. Birbilis, Int. Mater. Rev., 60 (2015) 169-194.
- 9 [45] L. Yang, N. Hort, D. Laipple, D. Höche, Y.D. Huang, K.U. Kainer, R. Willumeit, F.
10 Feyerabend, Acta Biomater., 9 (2013) 8475-8487.
- 11 [46] T.G. Sabbides, P.G. Koutsoukos, J. Cryst. Growth, 133 (1993) 13-22.
- 12 [47] M.M. Reddy, K.K. Wang, J. Cryst. Growth, 50 (1980) 470-480.
- 13 [48] A. Mucci, J.W. Morse, Geochim. Cosmochim. Acta, 47 (1983) 217-233.
- 14 [49] A. Katz, Geochim. Cosmochim. Acta, 37 (1973) 1563-1586.
- 15 [50] F.C. Meldrum, S.T. Hyde, J. Cryst. Growth, 231 (2001) 544-558.
- 16 [51] O. Söhnel, J.W. Mullin, J. Cryst. Growth, 60 (1982) 239-250.
- 17 [52] M. Jamesh, S. Kumar, T.S.N.S. Narayanan, Corros. Sci., 53 (2011) 645-654.
- 18 [53] P.L. Jiang, C. Blawert, N. Scharnagl, M.L. Zheludkevich, Corros. Sci., 153 (2019) 62-73.
- 19 [54] M.M. Avedesian, H. Baker, ASM pecialty handbook: magnesium and magnesium alloys,
20 ASM international, 1999, pp. 228-235.
- 21 [55] F. Yang, F. Lv, X.M. Yang, S.X. Li, Z.F. Zhang, Q.D. Wang, Mater. Sci. Eng. A, 528
22 (2011) 2231-2238.
- 23 [56] D. Bian, W.R. Zhou, Y. Liu, N. Li, Y.F. Zheng, Z.L. Sun, Acta Biomater., 41 (2016)
24 351-360.
- 25
- 26

Figure and table captions

- 1
- 2 **Table 1** Mechanical properties of Mg₄Zn_{0.2}Sn alloy at room temperature.
- 3 **Table 2** Mechanical properties of pre-corroded Mg₄Zn_{0.2}Sn alloy at room temperature.
- 4 **Fig. 1.** Microstructure of Mg₄Zn_{0.2}Sn alloy examined by (a) OM and (b, c) SEM in BSE
5 mode along the extrusion direction. (d) The inverse pole figure parallel to the extrusion
6 direction of Mg₄Zn_{0.2}Sn alloy (left: <0001>, upper right: <11-20>, lower right: <10-10>).
- 7 **Fig. 2.** Bode plots of the EIS spectra of Mg₄Zn_{0.2}Sn alloy tested in (a, b) NaCl-DIW and (c,
8 d) NaCl-ATW solutions.
- 9 **Fig. 3.** Polarization curves of Mg₄Zn_{0.2}Sn alloy measured in NaCl-DIW and NaCl-ATW
10 solutions.
- 11 **Fig. 4.** Surface and cross section morphologies of Mg₄Zn_{0.2}Sn alloy after immersion in (a, c)
12 NaCl-DIW and (b, d) NaCl-ATW solutions for 48 h.
- 13 **Fig. 5.** XRD analysis for the compositions of corrosion products formed on Mg₄Zn_{0.2}Sn
14 alloy surface after immersion in NaCl-DIW and NaCl-ATW solutions for 48 h.
- 15 **Fig. 6.** Engineering tensile and compressive strain-stress curves of Mg₄Zn_{0.2}Sn alloys tested
16 at room temperature.
- 17 **Fig. 7.** (a) Tensile stress-strain curves of Mg₄Zn_{0.2}Sn alloy after pre-corrosion in salt spray
18 for different time and (b) variation of tensile mechanical properties with pre-corrosion
19 duration.
- 20 **Fig. 8.** Macroscopic surface morphologies of Mg₄Zn_{0.2}Sn alloy imaged by optical
21 microscope after salt spray for different time.
- 22 **Fig. 9.** SEM fracture surfaces of Mg₄Zn_{0.2}Sn alloy after tensile tests at room temperature (a,
23 b, c) without exposure to salt spray and with exposure to salt spray for (d, e, f) 3 days, (g, h, i)
24 14 days and (j, k, l) 28 days.
- 25 **Fig. 10.** Stress-life (S-N) curves of Mg₄Zn_{0.2}Sn alloy measured in air, NaCl-DIW and NaCl-
26 ATW solutions.
- 27 **Fig. 11.** Fatigue fractography of Mg₄Zn_{0.2}Sn alloy after fatigue tests under stress amplitude
28 of (a, b, c, d) 155 MPa (27476.5 cycles) in air, (e, f, g, h) 120 MPa (2620869 cycles) in NaCl-
29 DIW solution and (i, j, k, l) 125 MPa (1976289 cycles) in NaCl-ATW solution
- 30 **Fig. 12.** Typical EDS analysis result of the inclusions in the fracture of Mg₄Zn_{0.2}Sn alloy
31 after fatigue tests in air.
- 32 **Fig. 13.** Fracture surfaces of Mg₄Zn_{0.2}Sn alloy after corrosion fatigue tests in NaCl-DIW
33 solution under stress amplitude of 120 MPa (failed after different cycles).
- 34
- 35
- 36

1
2
3
4
5
6
7
8
9
10

Table list:

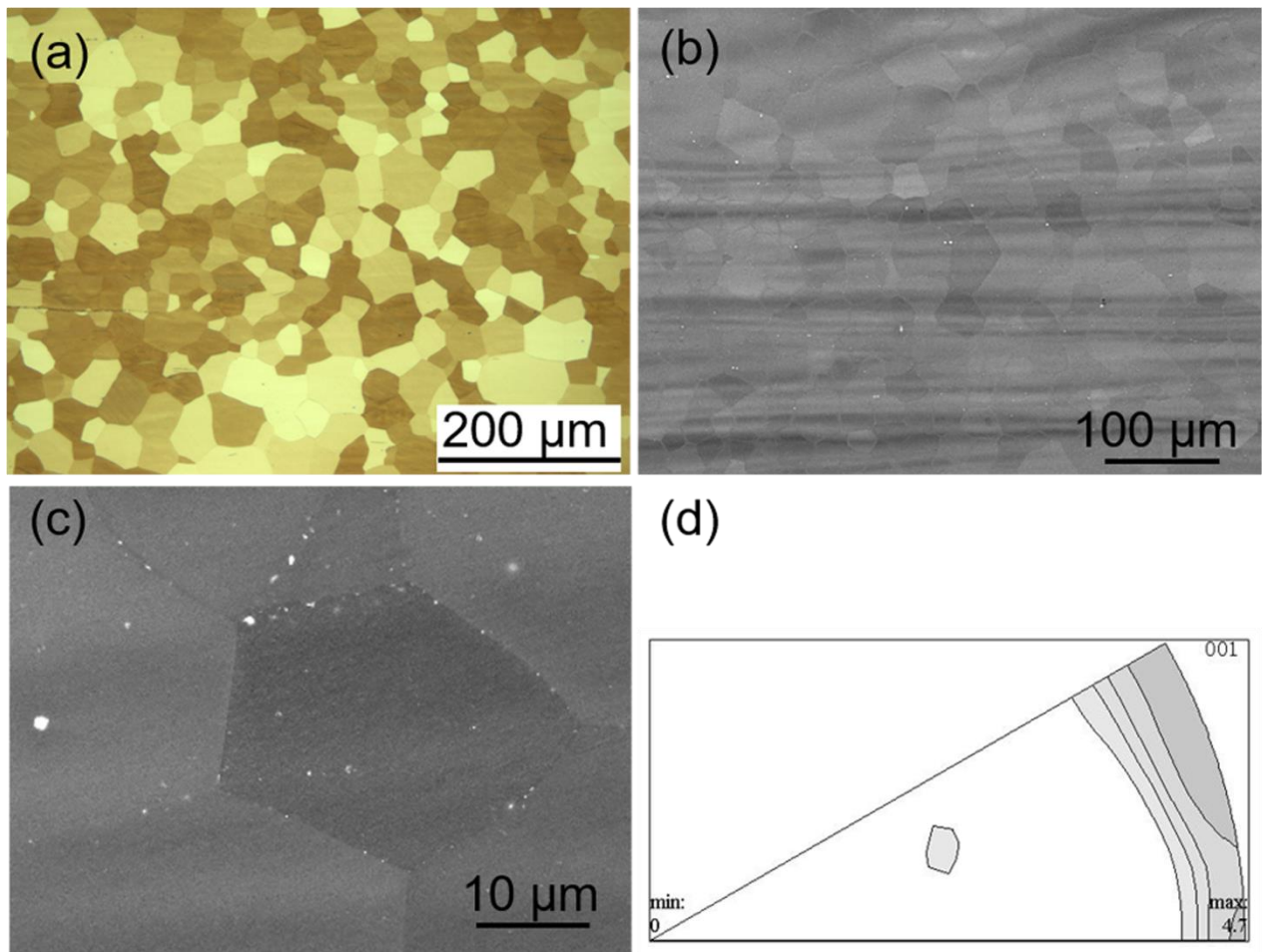
Table 1 Mechanical properties of Mg₄Zn_{0.2}Sn alloy at room temperature.

Tensile property			Compressive property		TYS/CYS
0.2% TYS / MPa	UTS / MPa	Elongation / %	0.2% CYS / MPa	UCS / MPa	
157 ± 0	254 ± 1	16 ± 1	80 ± 0	357 ± 2	2.0

Table 2 Mechanical properties of pre-corroded Mg₄Zn_{0.2}Sn alloy at room temperature.

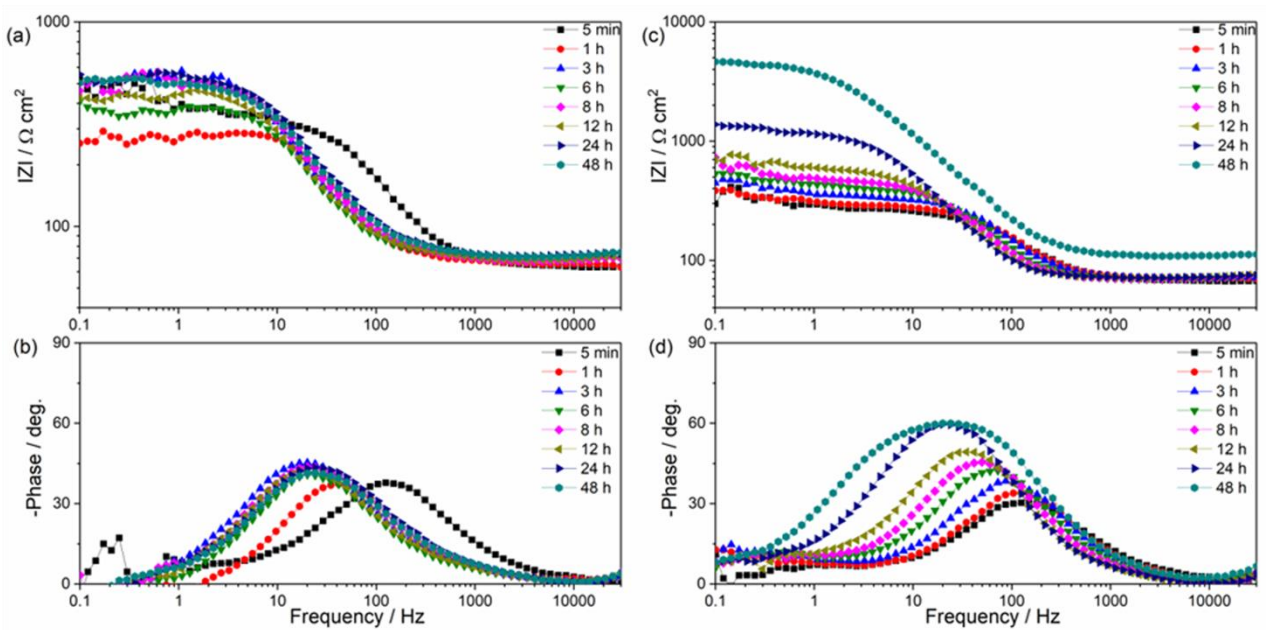
Salt spray duration / day	Tensile property		
	0.2% TYS / MPa	UTS / MPa	Elongation / %
0	157 ± 0	254 ± 1	16 ± 1
3	156 ± 1	248 ± 2	11 ± 1
7	153 ± 2	237 ± 7	10 ± 3
14	149 ± 2	216 ± 10	7 ± 1
28	136 ± 5	189 ± 2	4 ± 1

Figure list:



1
2
3
4
5

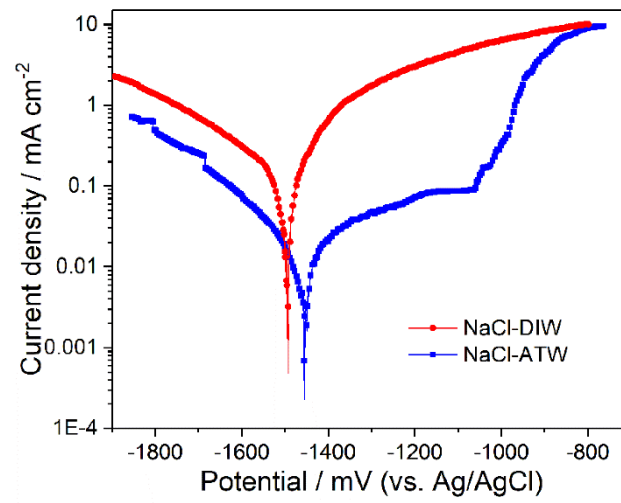
Fig. 1. Microstructure of Mg₄Zn_{0.2}Sn alloy examined by (a) OM and (b, c) SEM in BSE mode along the extrusion direction. (d) The inverse pole figure parallel to the extrusion direction of Mg₄Zn_{0.2}Sn alloy (left: <0001>, upper right: <11-20>, lower right: <10-10>).



6

1 **Fig. 2.** Bode plots of the EIS spectra of Mg₄Zn_{0.2}Sn alloy tested in (a, b) NaCl-DIW and (c,
2 d) NaCl-ATW solutions.

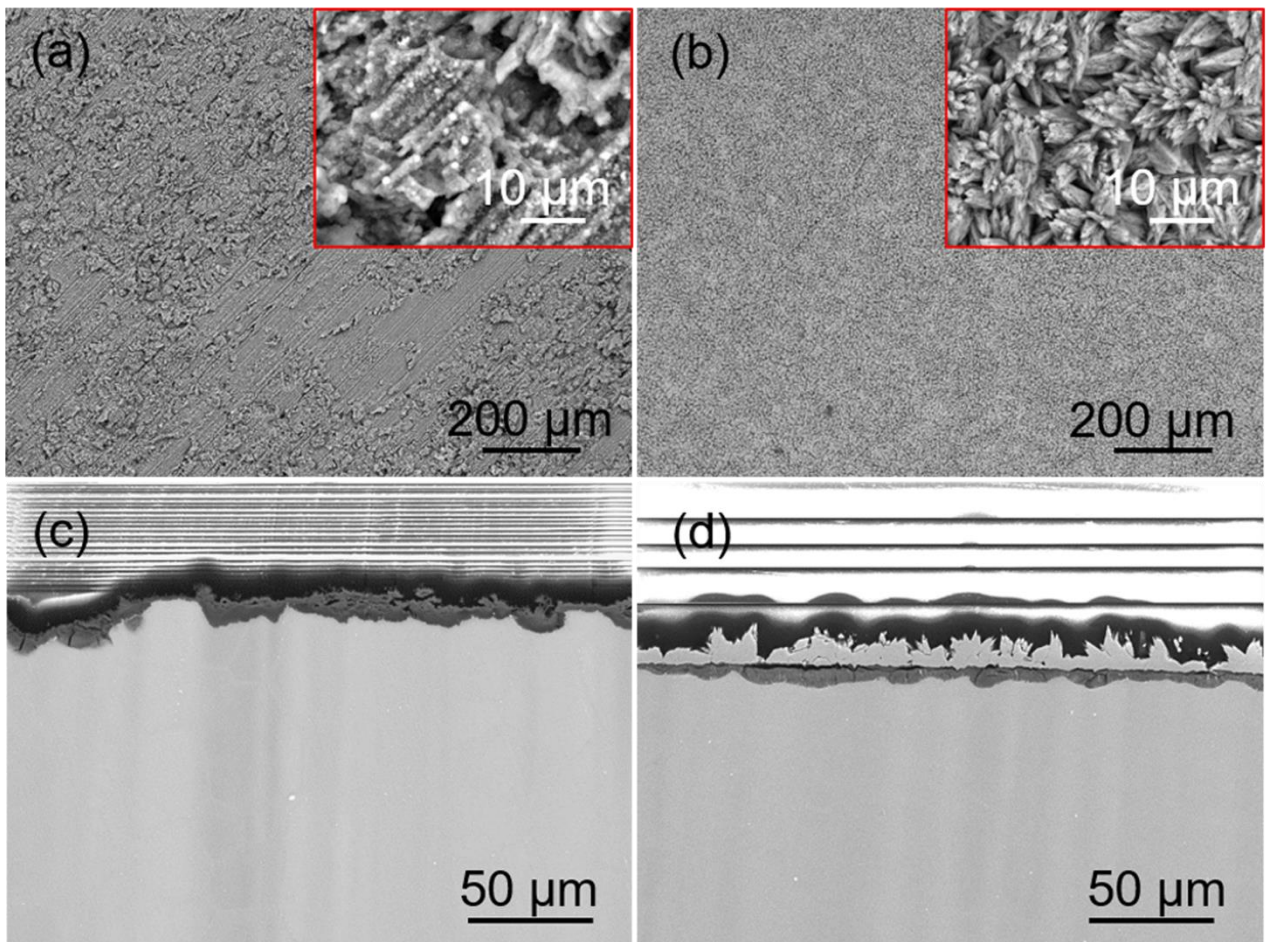
3



4

5 **Fig. 3.** Polarization curves of Mg₄Zn_{0.2}Sn alloy measured in NaCl-DIW and NaCl-ATW
6 solutions.

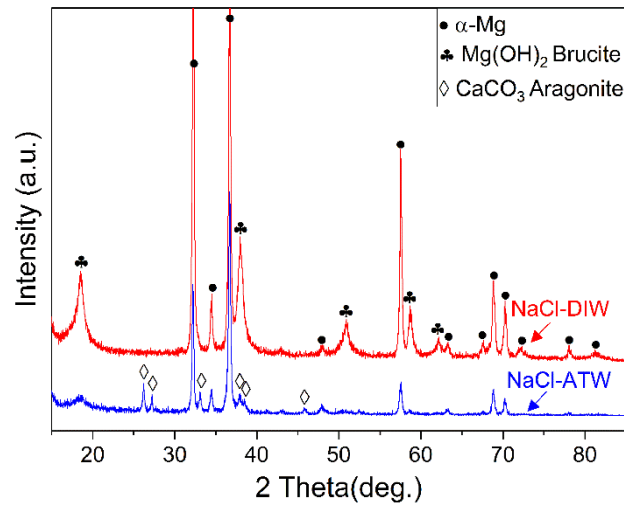
7



8

1 **Fig. 4.** Surface and cross section morphologies of Mg₄Zn_{0.2}Sn alloy after immersion in (a, c)
2 NaCl-DIW and (b, d) NaCl-ATW solutions for 48 h.

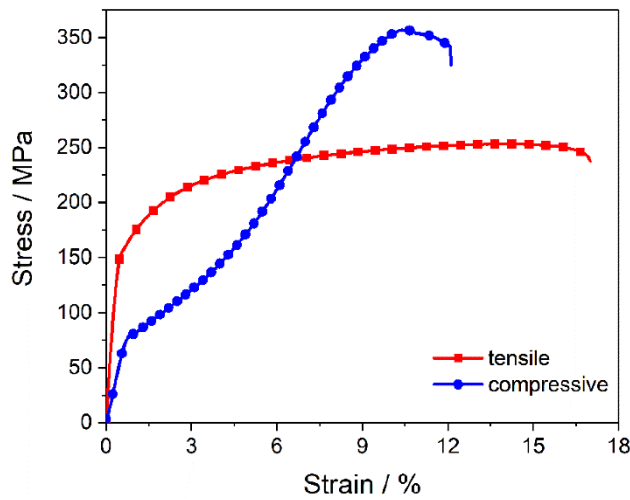
3



4

5 **Fig. 5.** XRD analysis for the compositions of corrosion products formed on Mg₄Zn_{0.2}Sn
6 alloy surface after immersion in NaCl-DIW and NaCl-ATW solutions for 48 h.

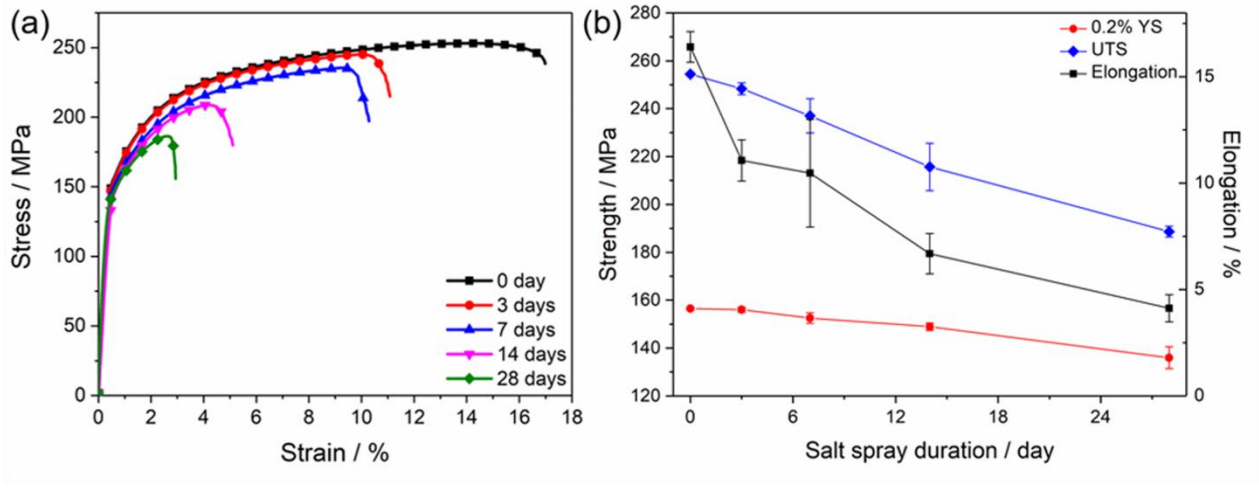
7



8

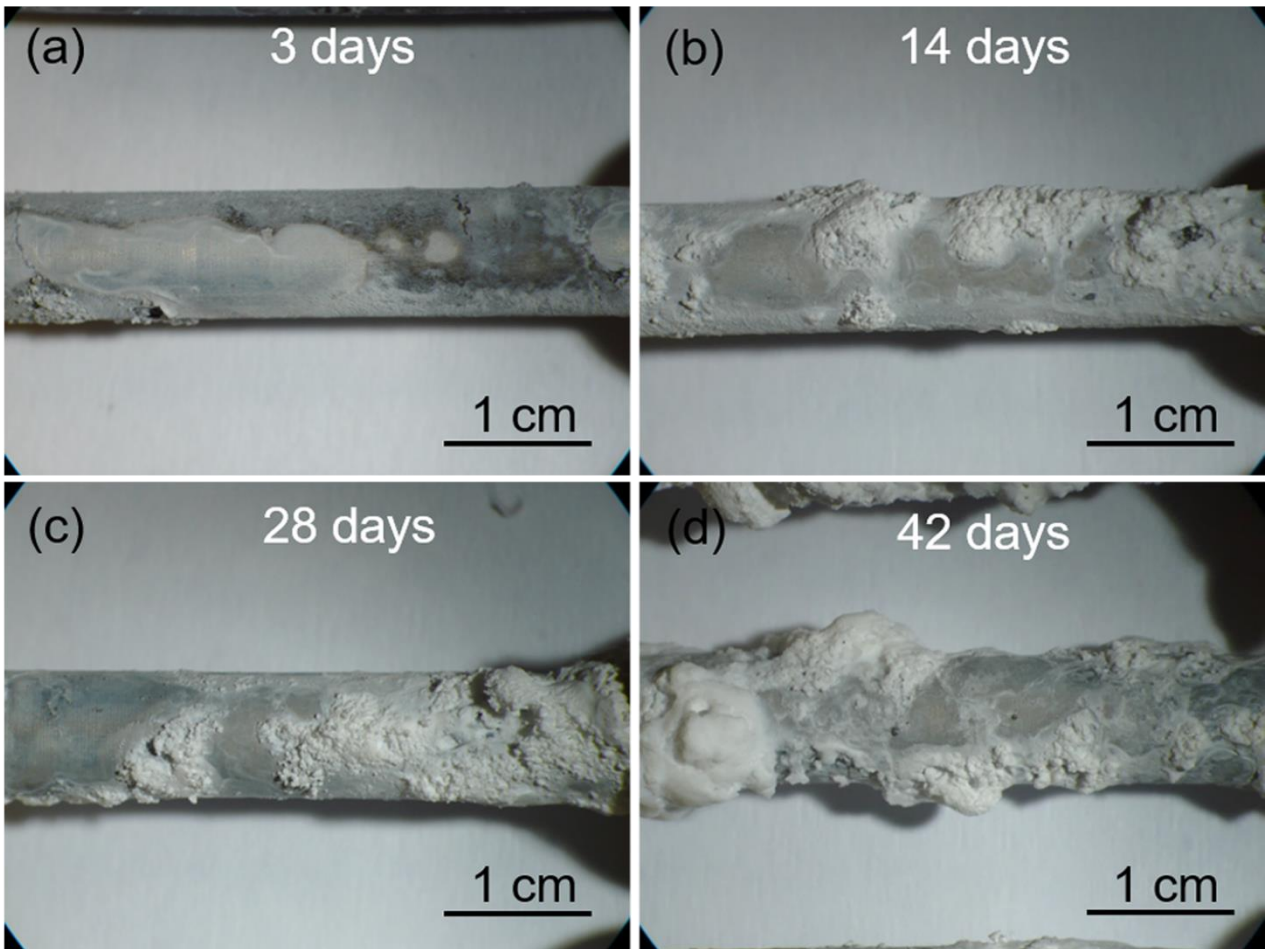
9 **Fig. 6.** Engineering tensile and compressive strain-stress curves of Mg₄Zn_{0.2}Sn alloys tested
10 at room temperature.

11



1
2
3
4
5

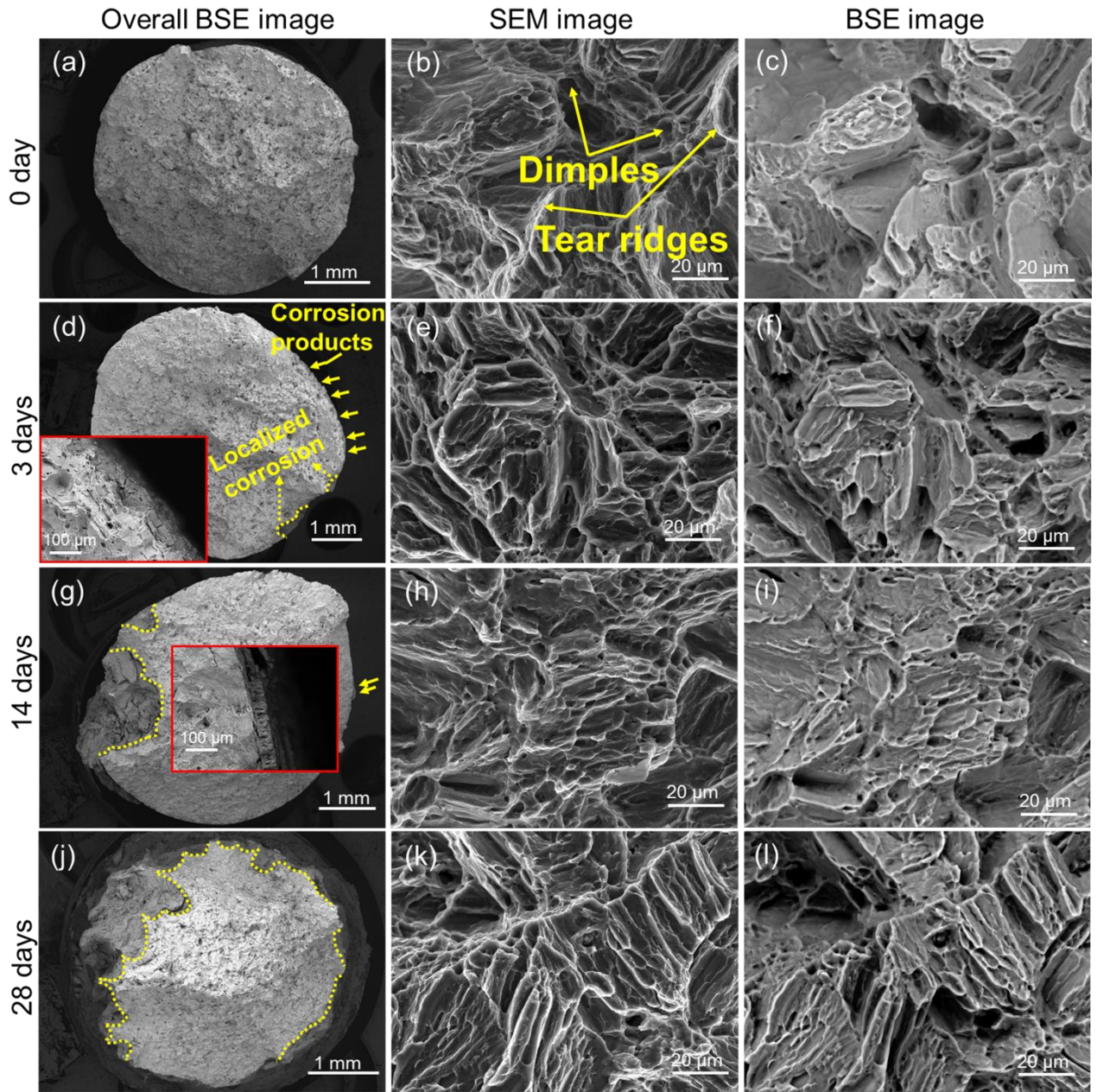
Fig. 7. (a) Tensile stress-strain curves of Mg₄Zn_{0.2}Sn alloy after pre-corrosion in salt spray for different time and (b) variation of tensile mechanical properties with pre-corrosion duration.



6
7
8

Fig. 8. Macroscopic surface morphologies of Mg₄Zn_{0.2}Sn alloy imaged by optical microscope after salt spray for different time.

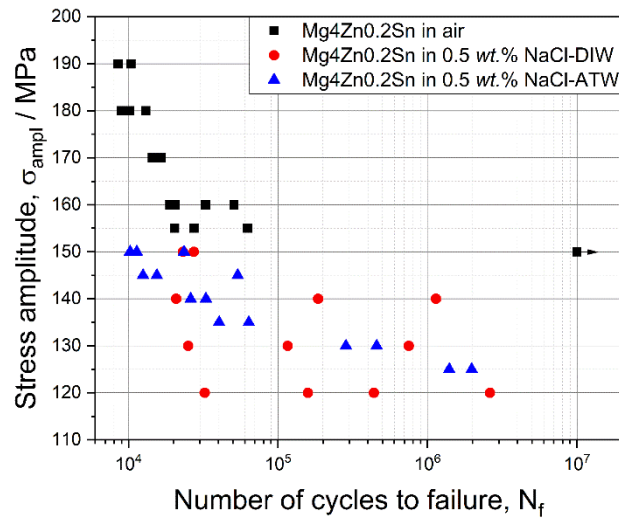
1



2

3 **Fig. 9.** SEM fracture surfaces of Mg₄Zn_{0.2}Sn alloy after tensile tests at room temperature (a,
4 b, c) without exposure to salt spray and with exposure to salt spray for (d, e, f) 3 days, (g, h, i)
5 14 days and (j, k, l) 28 days.

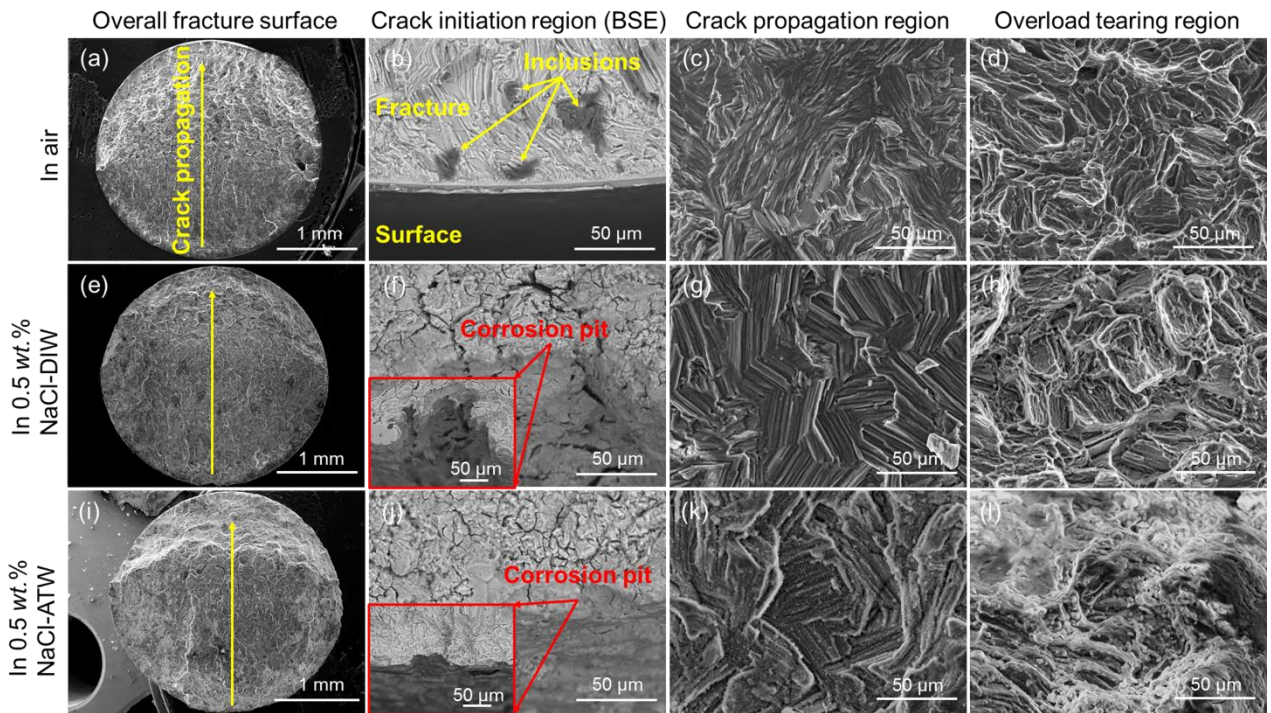
6



1

2 **Fig. 10.** Stress-life (S-N) curves of Mg4Zn0.2Sn alloy measured in air, NaCl-DIW and NaCl-
 3 ATW solutions.

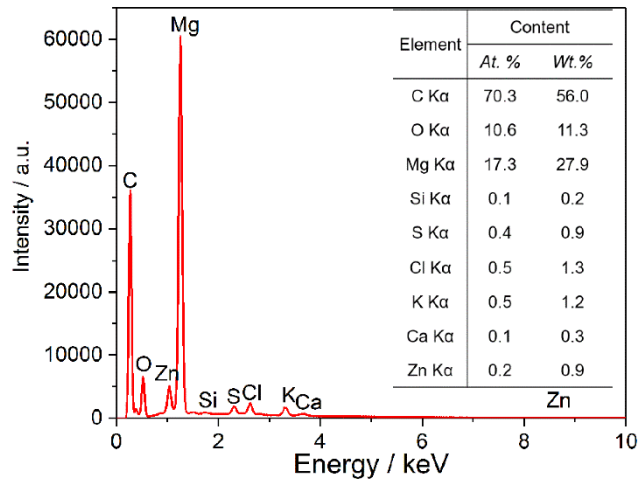
4



5

6 **Fig. 11.** Fatigue fractography of Mg4Zn0.2Sn alloy after fatigue tests under stress amplitude
 7 of (a, b, c, d) 155 MPa (27476.5 cycles) in air, (e, f, g, h) 120 MPa (2620869 cycles) in NaCl-
 8 DIW solution and (i, j, k, l) 125 MPa (1976289 cycles) in NaCl-ATW solution

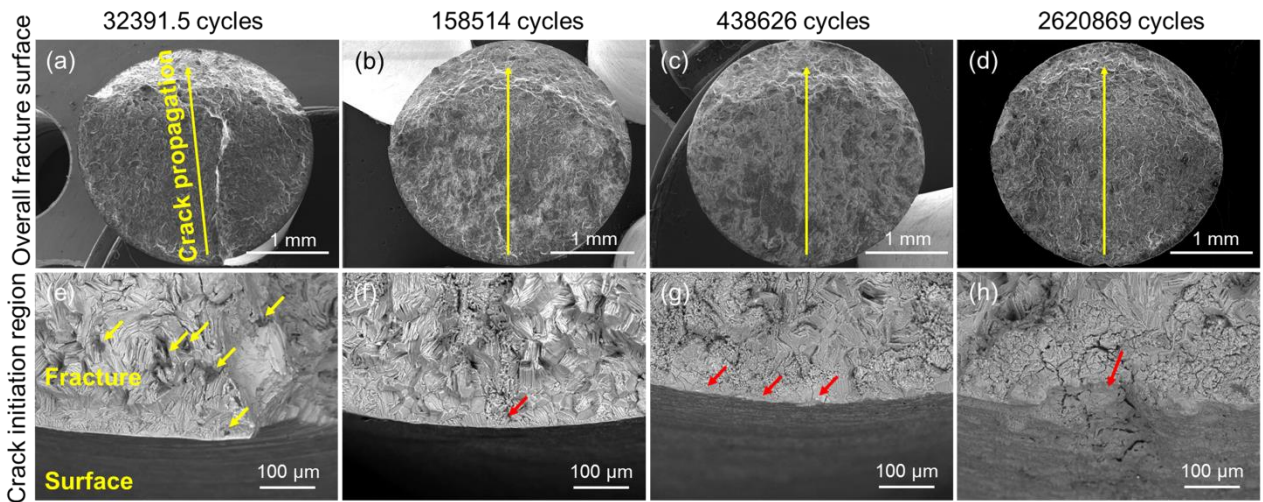
9



1

2 **Fig. 12.** Typical EDS analysis result of the inclusions in the fracture of Mg₄Zn_{0.2}Sn alloy
 3 after fatigue tests in air.

4



5

6 **Fig. 13.** Fracture surfaces of Mg₄Zn_{0.2}Sn alloy after corrosion fatigue tests in NaCl-DIW
 7 solution under stress amplitude of 120 MPa (failed after different cycles).

8